



## River computations: artificial backwater from the momentum advection scheme

Frank W. Platzek, Guus S. Stelling, Jacek A. Jankowski, Regina Patzwahl & Julie D. Pietrzak

To cite this article: Frank W. Platzek, Guus S. Stelling, Jacek A. Jankowski, Regina Patzwahl & Julie D. Pietrzak (2018): River computations: artificial backwater from the momentum advection scheme, Journal of Hydraulic Research, DOI: [10.1080/00221686.2017.1399935](https://doi.org/10.1080/00221686.2017.1399935)

To link to this article: <https://doi.org/10.1080/00221686.2017.1399935>



Published online: 05 Mar 2018.



Submit your article to this journal [↗](#)



Article views: 39



View related articles [↗](#)



View Crossmark data [↗](#)

Research paper

## River computations: artificial backwater from the momentum advection scheme

FRANK W. PLATZEK (IAHR member), PhD Student, *Deltares, Boussinesqweg 1, 2629 HV, Delft, the Netherlands*Email: [frank.platzek@deltares.nl](mailto:frank.platzek@deltares.nl) (author for correspondence)GUUS S. STELLING, Emeritus Professor, *Stelling Hydraulics, Binnenluiendijk 40, 1621 ME, Hoorn, the Netherlands*Email: [info@stellinghydraulics.com](mailto:info@stellinghydraulics.com)JACEK A. JANKOWSKI (IAHR member), Research Engineer, *Department of Hydraulic Engineering in Inland Areas, Federal Waterways Engineering and Research Institute (BAW), Kußmaulstraße 17, 76187, Karlsruhe, Germany*Email: [jacek.jankowski@baw.de](mailto:jacek.jankowski@baw.de)REGINA PATZWahl (IAHR member), Research Engineer, *Department of Hydraulic Engineering in Inland Areas, Federal Waterways Engineering and Research Institute (BAW), Kußmaulstraße 17, 76187, Karlsruhe, Germany*Email: [regina.patzwahl@baw.de](mailto:regina.patzwahl@baw.de)JULIE D. PIETRZAK, Professor, *Fluid Mechanics Section, Faculty of Civil Engineering and Geosciences, Delft University of Technology, Stevinweg 1, 2628 CN Delft, the Netherlands*Email: [j.d.pietrzak@tudelft.nl](mailto:j.d.pietrzak@tudelft.nl)

### ABSTRACT

The established method for determining dike heights and dimensioning river training structures is to assess the resulting backwater by numerical modelling. The common consensus is that bottom friction determines the backwater and that momentum advection only has a local effect. We demonstrate that the numerical/artificial backwater contribution from the momentum advection approximation can be of the same order of magnitude as the bottom friction contribution, depending on the advection scheme. This is realized using a one-dimensional analysis and verified using a set of one- and two-dimensional test problems including a wavy bed case, flow over emerged and submerged groynes and finally an actual river. We compare first- and second-order accurate advection schemes and compute their artificial contribution to the backwater, for a range of practically-feasible grid resolutions. The tests demonstrate that the conservation/constancy properties of the scheme determine the size of this contribution, rather than the order of the scheme.

**Keywords:** Artificial backwater; energy head; groyne; momentum advection; river; topography

### 1 Introduction

In many countries worldwide, costly river engineering projects aim at verifying the dike heights for flood protection or at dimensioning of river training structures (e.g. groynes) for ship navigation and bank protection. In such projects, the backwater needs to be determined with great certainty and accuracy, mostly by one- and two-dimensional numerical modelling. The backwater arises due to energy losses, commonly assumed to come from bottom friction and turbulent dissipation. However, computer models suffer from numerical errors, which reduce the accuracy of the solution. Such errors mostly originate from

the advection approximation for momentum transport, due to its nonlinearity. Here, one might ask: *Do these errors also affect the backwater?*

Most research on the numerical accuracy of advection schemes in shallow-water models is conducted using Godunov methods with Riemann solvers; see Toro and Garcia-Navarro (2007) for an overview. These approaches are particularly suited for capturing of shocks or discontinuities, e.g. in dambreak flows or hydraulic jumps. For accurate (quasi-) steady flow predictions over variable topography these schemes require being *well-balanced*, meaning that the flux terms and the source terms need to balance each other in the momentum

Received 7 January 2017; accepted 30 October 2017/Currently open for discussion.

equations; see e.g. Noelle, Xing, and Shu (2007), Caleffi and Valiani (2009), Ricchiuto (2015) and Caleffi, Valiani, and Li (2016) for some recent papers on this topic. These works successfully illustrate the accuracy, conservation and convergence properties of the applied methods using a number of commonly accepted academic test cases for such local phenomena (dambreak, flow over a bump, interacting shocks, etc.). However, many of these applications apply high-resolution grids, where the relevant (topographical) features are sufficiently resolved.

When considering large-scale river applications, with limited grid resolution (with respect to the topography), the local accuracy of the model and the capturing of possible discontinuities is often not feasible and also not the most critical issue. More important is the representation of the total energy loss in the system – resulting in the backwater – and the prediction of areas with increased velocity and bottom shear stress, e.g. for morphodynamic predictions. There may be locations in a model where one might expect energy losses in reality, but where the model lacks the required resolution to accurately represent the flow patterns causing them, e.g. for the flow over obstacles such as weirs or groynes. For this purpose, the numerical accuracy of the model needs to be investigated differently by focusing on the total flow resistance (physical and numerical).

To the authors' knowledge very few works have considered the numerical errors in this way. Canestrelli and Toro (2012) investigated a FORCE-type centred momentum advection scheme and found that different implementations of the scheme showed considerable differences in the backwater in a river reach, due to numerical diffusion from the advection discretization. This matches the findings of Stelling and Duinmeijer (2003), who examined a number of advection schemes, with different conservation/constancy properties, and showed how the head loss varies for the flow over sudden expansions, contractions and over a weir.

In this work, we continue these considerations and provide a new interpretation of discretization errors in numerical river modelling, introducing the concept of *artificial backwater*. We focus on real-world, quasi-steady river applications with complex geometry, using feasible grid resolution for engineering practice. The aim of this work is to determine the artificial contribution to the backwater and its dependence on the momentum advection approximation, for river applications with variable topography. We establish expressions for the contribution to the global backwater from errors in the advection scheme through an analysis of the steady inviscid momentum equation, also called the backwater or Bélanger equation; see e.g. Chanson (2004, 2009).

The results from this analysis are confirmed using a sequence of tests with flow over variable topography. A set of test problems was defined that increases in complexity towards a real-world case study of a 17 km stretch of the Elbe River in Germany. Applying a vertically-integrated, two-dimensional model, we perform three schematic, actually one-dimensional

(1D) tests, investigating the effect of a wavy bed, as well as two schematic two-dimensional (2D) tests with flow around and over groynes, and finally the case study of the Elbe River itself. In order to diminish errors due to the grid structure, we consider simple rectangular grids, allowing us to compare the effect of the advection scheme, exclusively.

In Section 2, we introduce the investigated momentum advection schemes, for which we analyse the artificial backwater contributions using a 1D analysis in Section 3. We describe the test cases in Section 4 and present the results in Section 5. We end with a discussion and conclusions in Sections 6 and 7.

## 2 Momentum advection discretizations

The modelling systems used for real-world river applications are often based on (semi-)implicit, staggered grid, finite-difference methods: e.g. POM (Blumberg & Mellor, 1987), UnTRIM (Casulli & Walters, 2000), Suntans (Fringer, Gerritsen, & Street, 2006), Delft3D (Deltares, 2011), MIKE 21 (DHI, 2011) and HEC-RAS (Brunner, 2016). Due to the implicit treatment of the pressure terms, the Courant number for stability is only based on the flow velocity  $u$  and not on the wave celerity  $c = (gH)^{1/2}$ . For this reason – for low-Froude number, quasi-steady river computations – these approaches allow the application of relatively large time steps and suffer from numerical diffusion that only scales with  $u$  and not with  $u \pm c$ .

The (nonlinear) momentum advection schemes in the aforementioned models are often extensions/combinations of several basic upwind schemes. In this section, we present a number of such schemes, which have been chosen for their different properties and complexities. The schemes have been implemented and tested in a two-dimensional, depth-averaged shallow-water solver (Platzek, Stelling, Jankowski, Patzwahl, & Pietrzak, 2016). For the present investigations, the contributions due to horizontal diffusion, Coriolis and wind are neglected. The momentum and continuity equations then read:

$$\frac{\partial u}{\partial t} + u \frac{\partial u}{\partial x} + v \frac{\partial u}{\partial y} + g \frac{\partial \zeta}{\partial x} + \frac{\gamma |U| u}{H} = 0 \quad (1)$$

$$\frac{\partial v}{\partial t} + u \frac{\partial v}{\partial x} + v \frac{\partial v}{\partial y} + g \frac{\partial \zeta}{\partial y} + \frac{\gamma |U| v}{H} = 0 \quad (2)$$

$$\frac{\partial \zeta}{\partial t} + \frac{\partial (Hu)}{\partial x} + \frac{\partial (Hv)}{\partial y} = 0 \quad (3)$$

where  $u$  and  $v$  are the depth-averaged velocities in the  $x$ - and  $y$ -directions;  $\zeta$  is the free-surface position;  $H$  is the total water depth defined as  $H = \zeta - h$ , where  $h$  is the bed level;  $t$  represents time;  $g$  is the gravitational acceleration and  $\gamma$  is the bottom friction coefficient, computed using e.g. a Chézy, Manning or Nikuradse roughness formulation and  $|U| = (u^2 + v^2)^{1/2}$ .

The equations are discretized on a uniform Cartesian grid, with grid sizes  $\Delta x$  and  $\Delta y$ . The grid has  $I$  cells in the  $x$ -direction and  $J$  cells in the  $y$ -direction. We use a C-grid administration (staggered positioning of variables), i.e. the water level  $\zeta$  is specified in cell centres and the velocity components  $u$  and  $v$  at cell edges (Fig. 1 has a 1D representation).  $\Omega_{i,j}$  is the cell at position  $(i,j)$ , where  $i$  and  $j$  are the indices in  $x$  and  $y$ -direction, respectively, with  $i = 1, 2, \dots, I; j = 1, 2, \dots, J$ . We discretize the momentum equation (Eq. (1)) for each cell edge  $\Gamma_{i+1/2,j}$  using a semi-implicit time discretization where the advection term is treated explicitly and both the free-surface gradient and the bottom friction term are discretized implicitly (see e.g. Casulli, 1990; Casulli & Cattani, 1994):

$$\frac{u_{i+1/2,j}^{n+1} - u_{i+1/2,j}^n}{\Delta t} + Fu_{i+1/2,j}^n + g \frac{\zeta_{i+1,j}^{n+1} - \zeta_{i,j}^{n+1}}{\Delta x} + \frac{\gamma_{i+1/2,j}^n}{H_{i+1/2,j}^n} |u_{i+1/2,j}^{n+1}| u_{i+1/2,j}^{n+1} = 0 \quad (4)$$

where  $n$  is the time level and  $\Delta t$  is the time step size. On the uniform rectangular grid, the central discretization for the pressure gradient in Eq. (4) is second-order accurate. The depth in the velocity point  $H_{i+1/2}^n$  used in the friction term is also approximated using central averaging. The operator  $Fu_{i+1/2,j}^n$  contains the explicit discretization of the momentum advection term and is the subject of the present investigation. The momentum equation in the  $y$ -direction (Eq. (2)) is discretized similarly.

We investigate the effect on the backwater of three first-order and two second-order accurate discretizations for the advective operator  $Fu$  (and  $Fv$ ):

- (1) First-order upwind (FOU)
- (2) First-order upwind, momentum conservative (FOU-MC-E)
- (3) First-order upwind, with energy-head constancy (FOU-EHC)
- (4) Second-order upwind (SOU)
- (5) Second-order upwind, momentum conservative (SOU-MC-E)

For brevity, only the discretization of the longitudinal advection term  $u\partial u/\partial x$  as in a 1D model (leaving out the cross-advection

term  $v\partial u/\partial y$ ) is presented. Similar expressions hold for the discretization of  $Fv$  in two dimensions. The three first-order schemes can be written in the following general form:

$$Fu_{i+1/2,j}^n = u_{i+1,j}^+ \frac{u_{i+3/2,j}^n - u_{i+1/2,j}^n}{\Delta x} + u_{i,j}^- \frac{u_{i+1/2,j}^n - u_{i-1/2,j}^n}{\Delta x} \quad (5)$$

The definition of the advective velocities  $u_{i+1,j}^+$  and  $u_{i,j}^-$  determines the properties of the scheme.

## 2.1 First order upwind (FOU)

This is the simplest upwind discretization.

The advection term is computed using Eq. (5), where the advective velocities are simply taken first-order upwind:

$$u_{i+1,j}^+ = \begin{cases} 0 & \text{if } u_{i+1/2,j}^n \geq 0 \\ u_{i+1/2,j}^n & \text{if } u_{i+1/2,j}^n < 0 \end{cases} \quad (6)$$

$$u_{i,j}^- = \begin{cases} u_{i+1/2,j}^n & \text{if } u_{i+1/2,j}^n > 0 \\ 0 & \text{if } u_{i+1/2,j}^n \leq 0 \end{cases} \quad (7)$$

For positive flow direction ( $u_{i+1/2,j}^n > 0$ ), insertion of these advective velocities in Eq. (5) results in:

$$Fu_{i+1/2,j}^n = u_{i+1/2,j}^n \frac{u_{i+1/2,j}^n - u_{i-1/2,j}^n}{\Delta x} \quad (8)$$

## 2.2 First order upwind, momentum conservative (FOU-MC-E)

In this discretization, which was introduced in Stelling and Duinmeijer (2003), a conservative finite volume formulation is rewritten to a simple finite difference method with the same properties. The method was extended to unstructured grids based on the work by Perot (2000) in Kramer and Stelling (2008) and applied and further developed in Kernkamp, van Dam, Stelling, and de Goede (2011) and Kleptsova, Pietrzak, and Stelling (2012). It was applied in combination with high-resolution subgrid topography by Stelling (2012) (on quadtree grids) and Volp, van Prooijen, and Stelling (2013). With the chosen semi-implicit temporal discretization, it can

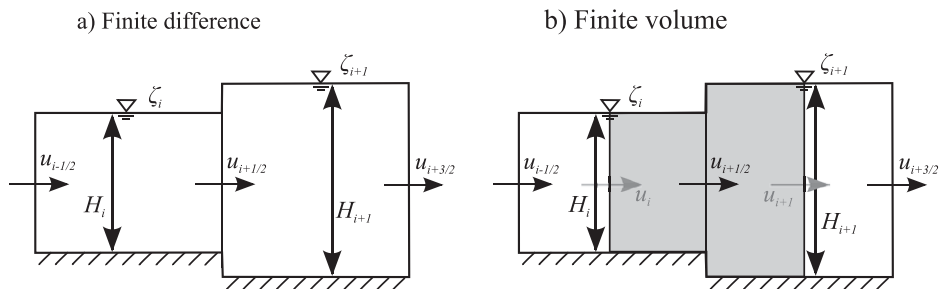


Figure 1 The staggered 1D stencil with water level  $\zeta$  and total depth  $H$  in the cell centres and velocity  $u$  and at the edges. (a) The finite difference stencil. (b) The finite volume stencil with the velocity volume (grey area) and the cell centre velocities  $u_i$  (grey vectors)

only be demonstrated to be momentum conservative on a discrete level for stationary conditions. It is derived by rewriting the advection term from Eq. (1) into:

$$u \frac{\partial u}{\partial x} = \frac{1}{H} \left( \frac{\partial (qu)}{\partial x} - u \frac{\partial q}{\partial x} \right) \quad (9)$$

where  $q = Hu$  is the specific discharge. Discretizing for edge  $\Gamma_{i+1/2,j}$  at time level  $n$ , we get:

$$Fu_{i+1/2,j}^n = \frac{1}{\bar{H}_{i+1/2,j}^n} \times \left( \frac{\bar{q}_{i+1,j}^x u_{i+1,j}^* - \bar{q}_{i,j}^x u_{i,j}^*}{\Delta x} - u_{i+1/2,j} \frac{\bar{q}_{i+1,j}^x - \bar{q}_{i,j}^x}{\Delta x} \right) \quad (10)$$

where

$$\begin{aligned} \bar{q}_{i,j}^x &= \frac{1}{2} (q_{i-1/2,j}^x + q_{i+1/2,j}^x) \\ &= \frac{1}{2} (H_{i-1/2,j}^* u_{i-1/2,j}^n + H_{i+1/2,j}^* u_{i+1/2,j}^n) \end{aligned} \quad (11)$$

$$\bar{H}_{i+1/2,j}^n = \frac{1}{2} (H_{i,j}^n + H_{i+1,j}^n) \quad (12)$$

$$H_{i+1/2,j}^* = \begin{cases} \zeta_{i,j}^n - h_{i+1/2,j}^n & \text{if } u_{i+1/2,j}^n \geq 0 \\ \zeta_{i+1,j}^n - h_{i+1/2,j}^n & \text{if } u_{i+1/2,j}^n < 0 \end{cases} \quad (13)$$

$$u_{i,j}^* = \begin{cases} u_{i-1/2,j}^n & \text{if } u_{i-1/2,j}^n + u_{i+1/2,j}^n \geq 0 \\ u_{i+1/2,j}^n & \text{if } u_{i-1/2,j}^n + u_{i+1/2,j}^n < 0 \end{cases} \quad (14)$$

For flow in the positive  $x$ -direction, this simplifies to the following advection term:

$$u \frac{\partial u}{\partial x} \Big|_{i+1/2}^n = \frac{q_{i-1/2,j}^x + q_{i+1/2,j}^x}{H_{i,j}^n + H_{i+1,j}^n} \frac{u_{i+1/2}^n - u_{i-1/2}^n}{\Delta x} \quad (15)$$

The advective velocities in (5) for this scheme are thus computed as:

$$u_{i+1,j}^+ = \begin{cases} 0 & \text{if } u_{i+1/2,j}^n + u_{i+3/2,j}^n \geq 0 \\ \frac{q_{i+1/2,j}^x + q_{i+3/2,j}^x}{H_{i,j}^n + H_{i+1,j}^n} & \text{if } u_{i+1/2,j}^n + u_{i+3/2,j}^n < 0 \end{cases} \quad (16)$$

$$u_{i,j}^- = \begin{cases} \frac{q_{i-1/2,j}^x + q_{i+1/2,j}^x}{H_{i,j}^n + H_{i+1,j}^n} & \text{if } u_{i-1/2,j}^n + u_{i+1/2,j}^n > 0 \\ 0 & \text{if } u_{i-1/2,j}^n + u_{i+1/2,j}^n \leq 0 \end{cases} \quad (17)$$

where  $q_{i+1/2,j}^x = Q_{i+1/2,j}^n / \Delta y$  is the specific discharge in  $x$ -direction. The detailed derivation can be found in Stelling and Duinmeijer (2003).

### 2.3 First order upwind, with energy-head constancy (FOU-EHC)

This discretization was also introduced in Stelling and Duinmeijer (2003) and applied in Kramer and Stelling (2008) and Platzeck et al. (2016). The advection is again expressed as Eq. (5), and the advective velocities are computed as:

$$u_{i+1,j}^+ = \begin{cases} 0 & \text{if } u_{i+1/2,j}^n + u_{i+3/2,j}^n \geq 0 \\ -\frac{1}{2} (u_{i+1/2,j}^n + u_{i+3/2,j}^n) & \text{if } u_{i+1/2,j}^n + u_{i+3/2,j}^n < 0 \end{cases} \quad (18)$$

$$u_{i,j}^- = \begin{cases} \frac{1}{2} (u_{i-1/2,j}^n + u_{i+1/2,j}^n) & \text{if } u_{i-1/2,j}^n + u_{i+1/2,j}^n > 0 \\ 0 & \text{if } u_{i-1/2,j}^n + u_{i+1/2,j}^n \leq 0 \end{cases} \quad (19)$$

For positive flow direction ( $u_{i+1/2,j}^n > 0$ ), insertion of these advective velocities in Eq. (5) results in:

$$\begin{aligned} Fu_{i+1/2,j}^n &= \frac{u_{i-1/2,j}^n + u_{i+1/2,j}^n}{2} \frac{u_{i+1/2,j}^n - u_{i-1/2,j}^n}{\Delta x} \\ &= \frac{\frac{1}{2} (u_{i+1/2,j}^n)^2 - \frac{1}{2} (u_{i-1/2,j}^n)^2}{\Delta x} \end{aligned} \quad (20)$$

Combined with a central discretization of the pressure gradient, this scheme keeps the energy head  $\zeta_{i,j} + u_{i-1/2,j}^2 / (2g)$  (note the shifted indices) constant along streamlines without introducing any backwater. The analysis in Section 3 and the numerical tests in Section 4 confirm this property.

### 2.4 Second-order upwind (SOU)

This scheme is the extension of the first order upwind scheme in Section 2.1, based on inclusion of an extra term from the Taylor series expansion. It cannot be written in the general form of the first-order schemes (Eq. (5)). Instead the discretization reads:

$$\begin{aligned} Fu_{i+1/2,j}^n &= -\frac{1}{\Delta x} [u_{i+1,j}^* (u_{i+5/2,j}^n - 4u_{i+3/2,j}^n + 3u_{i+1/2,j}^n) \\ &\quad + u_{i,j}^* (3u_{i+1/2,j}^n - 4u_{i-1/2,j}^n + u_{i-3/2,j}^n)] \end{aligned} \quad (21)$$

with advective velocities  $u_{i+1}^*$  and  $u_i^*$ :

$$u_{i+1,j}^* = \begin{cases} 0 & \text{if } u_{i+1/2,j}^n \geq 0 \\ u_{i+1/2,j}^n & \text{if } u_{i+1/2,j}^n < 0 \end{cases} \quad (22)$$

$$u_{i,j}^* = \begin{cases} u_{i+1/2,j}^n & \text{if } u_{i+1/2,j}^n > 0 \\ 0 & \text{if } u_{i+1/2,j}^n \leq 0 \end{cases} \quad (23)$$

This scheme can be shown to be second-order accurate in space on a regular grid.

### 2.5 Second order upwind, momentum conservative (SOU-MC-E)

The scheme from Section 2.2 can be improved by using second-order accurate interpolation with a slope limiter (see e.g. Stelling & Duinmeijer, 2003), to compute both the upwind value for  $u_{i,j}^*$  at the cell centre and the water level  $\zeta_{i+1/2}^*$  needed at the cell face to compute the total depth  $H_{i+1/2}$ . In practice, the slope limiter makes sure that the scheme reduces to first order when there is large local variation of the gradients. In the end, only the computation of the upwind expressions for  $H_{i+1/2}^n$  and for  $u_{i,j}^*$  is modified:

$$H_{i+1/2}^n = \zeta_{i+1/2}^* - h_{i+1/2}^n \quad (24)$$

$$\zeta_{i+1/2}^* = \begin{cases} \zeta_{i,j}^n + \frac{1}{2}\psi(r_+^n)(\zeta_{i,j}^n - \zeta_{i-1,j}^n) & \text{if } u_{i+1/2}^n \geq 0 \\ \zeta_{i+1,j}^n - \frac{1}{2}\psi(r_-^n)(\zeta_{i+2,j}^n - \zeta_{i+1,j}^n) & \text{if } u_{i+1/2}^n < 0 \end{cases} \quad (25)$$

$$r_+^n = \frac{\zeta_{i+1,j}^n - \zeta_{i,j}^n}{\zeta_{i,j}^n - \zeta_{i-1,j}^n}, \quad r_-^n = \frac{\zeta_{i+1,j}^n - \zeta_{i,j}^n}{\zeta_{i+2,j}^n - \zeta_{i+1,j}^n} \quad (26)$$

$$u_{i,j}^* = \begin{cases} u_{i-1/2,j}^n + \frac{1}{2}\psi(r_+^n)(u_{i-1/2,j}^n - u_{i-3/2,j}^n) & \text{if } u_{i-1/2,j}^n + u_{i+1/2,j}^n \geq 0 \\ u_{i+1/2,j}^n - \frac{1}{2}\psi(r_-^n)(u_{i+3/2,j}^n - u_{i+1/2,j}^n) & \text{if } u_{i-1/2,j}^n + u_{i+1/2,j}^n < 0 \end{cases} \quad (27)$$

$$r_+^n = \frac{u_{i+1/2,j}^n - u_{i-1/2,j}^n}{u_{i-1/2,j}^n - u_{i-3/2,j}^n}, \quad r_-^n = \frac{u_{i+1/2,j}^n - u_{i-1/2,j}^n}{u_{i+3/2,j}^n - u_{i+1/2,j}^n} \quad (28)$$

For the evaluation of the limiter function  $\psi$  many variants are known from the literature, see e.g. Zhang, Jiang, Liang, and Cheng (2015). We have implemented and tested several (MinMod, Van Leer, Koren, Monotonized Central, etc.), but the MinMod limiter showed the least restriction on the time step for stability and is applied in the present work:

$$\psi(r^n) = \max(0, \min(1, r^n)) \quad (29)$$

For the water levels  $\zeta$  the expression is defined accordingly.

### 3 Advection scheme analysis

The differential and integral forms of the governing equations are strictly energy-conservative and – when no discontinuities are present – this should not be affected by the momentum advection term. Unfortunately, discretization errors in the advection scheme lead to numerical diffusion. Here, we analyse

the momentum equation (Eq. (4)) and determine the artificial contribution to the backwater due to these discretization errors. For simplicity, we only analyse the three first-order accurate schemes from Section 2. We restrict ourselves to steady, inviscid, 1D flow and consider only flow in the positive direction ( $u > 0$ ).

The FOU and FOU-EHC scheme are strict finite difference schemes, whereas the FOU-MC-E scheme is derived from a finite volume scheme (Fig. 1). For the purpose of performing a general analysis for the three schemes, we define left (L) and right (R) velocities as follows:

$$\begin{aligned} \text{FOU/FOU-EHC} : u_L &= u_{i-1/2}, \quad u_R = u_{i+1/2} \\ \text{FOU-MC-E} : u_L &= u_i, \quad u_R = u_{i+1} \end{aligned} \quad (30)$$

where we leave the actual definition of the cell centre velocities  $u_i$  and  $u_{i+1}$  open. The water levels for all three schemes are defined as  $\zeta_L = \zeta_i$  and  $\zeta_R = \zeta_{i+1}$ . In this way, the schemes can be written in a general form and Eq. (4) reduces to (dropping the time level  $n$  since we have assumed a steady state):

$$(\alpha u_L + (1 - \alpha)u_R) \frac{u_R - u_L}{\Delta x} + g \frac{\zeta_R - \zeta_L}{\Delta x} = 0 \quad (31)$$

with coefficient  $\alpha$ :

$$\begin{aligned} \text{FOU} : \alpha &= 0 \\ \text{FOU-EHC} : \alpha &= \frac{1}{2} \\ \text{FOU-MC-E} : \alpha &= u_R / (u_L + u_R) \end{aligned} \quad (32)$$

where the expression for  $\alpha$  for the FOU-MC-E scheme was obtained using the definition  $q = Hu$ , providing  $\alpha = H_L / (H_L + H_R) = u_R / (u_L + u_R)$ .

Now we integrate the momentum equation over all cells in the  $x$ -direction and scale with  $g$  to obtain an expression with the dimension of the energy head in (m):

$$M = \frac{\Delta x}{g} \sum_{i=1}^I \left[ (\alpha u_L + (1 - \alpha)u_R) \frac{u_R - u_L}{\Delta x} + g \frac{\zeta_R - \zeta_L}{\Delta x} \right] \quad (33)$$

where  $M$  is the integral of the momentum equation, which can be rewritten as  $M = \Delta H + \Delta H^{\text{ADV}}$  (where ADV denotes the chosen advection scheme), to give the backwater  $\Delta H$  in terms of the energy head  $\zeta + u^2 / (2g)$ :

$$\begin{aligned} M &= \frac{1}{g} \sum_{i=1}^I \left[ \left( g\zeta_L + \frac{1}{2}u_L^2 \right) - \left( g\zeta_R + \frac{1}{2}u_R^2 \right) \right] \\ &\quad + \frac{1}{g} \sum_{i=1}^I \left[ \left( \frac{1}{2} - \alpha \right) u_L^2 + \left( \frac{1}{2} - \alpha \right) u_R^2 + (2\alpha - 1)u_L u_R \right] \end{aligned} \quad (34)$$

where the first term on the right is a conservative discretization of the gradient of the energy head, which does not contribute to



the backwater. The term on the second line forms the artificial backwater contribution from the advection term. We can inspect its value for different  $\alpha$ . It can easily be seen that for FOU-EHC scheme (with  $\alpha = 1/2$ ), the total head loss is zero:  $\Delta H^{\text{ADV}} = \Delta H^{\text{FOU-EHC}} = 0$  and the advection term has no contribution to the backwater, as was expected for this scheme.

For  $\alpha = 0$  (the FOU scheme), the backwater contribution  $\Delta H$  becomes:

$$\Delta H^{\text{FOU}} = \frac{1}{2g} \sum_{i=1}^I (u_L - u_R)^2 \quad (35)$$

which is identical to the sum of all Carnot losses over the channel (without contraction/expansion coefficient); see e.g. Chanson (2004).

This term is quadratic and, therefore, the artificial backwater contribution from advection for the FOU scheme is always positive.

The same analysis can be done for the FOU-MC-E scheme. Inserting  $\alpha$  from Eq. (32) in Eq. (34) and rearranging, we obtain:

$$\Delta H^{\text{FOU-MC-E}} = \frac{1}{2g} \sum_{i=1}^I \frac{(u_L - u_R)^3}{u_L + u_R} \quad (36)$$

We can compare the sign and size of Eqs (36) and (35) by computing the ratio  $\lambda$  between the local artificial head loss for the FOU-MC-E and FOU scheme:

$$\lambda_{i+1/2} = \frac{\Delta H_{i+1/2}^{\text{FOU-MC-E}}}{\Delta H_{i+1/2}^{\text{FOU}}} = \frac{u_L - u_R}{u_L + u_R} \quad (37)$$

Since we assumed positive flow direction, this ratio is always smaller than 1 and therefore the backwater from the FOU-MC-E scheme is always less than that from the FOU scheme. Moreover, the ratio is positive for  $u_L > u_R$ , i.e. for expansions and it is negative for  $u_L < u_R$ , i.e. for contractions. In other words, for local contractions, the FOU-MC-E advection scheme gives a negative contribution to the backwater, i.e. the advection term causes an erroneous increase in energy head, as already recognized by Stelling and Duinmeijer (2003) and Kramer and Stelling (2008) for the flow over sudden contractions (flow over a saw-tooth bottom and over a weir).

In line with Stelling and Duinmeijer (2003) and Kramer and Stelling (2008), one can conclude that for (strong) local contractions with sudden flow variation, the hydrostatic pressure assumption is not valid and Eq. (4) should be applied with care. In such flow situations, switching locally between the FOU-EHC (at contractions) and the FOU-MC-E scheme (elsewhere), provides more physically correct results.

## 4 Numerical experiments

We now aim to verify the findings from Section 3 using numerical experiments and quantify the contribution to the

backwater or total head loss due to the advection discretization for the flow over variable topography. As a reference, we take an existing numerical model for a stretch of the Elbe River, between the German cities of Lauenburg and Geesthacht (Platzeck et al., 2016). From this model, we construct a series of tests with increasing complexity, that schematically represents the geometrical variation along the river stretch: the overall bed slope, bed forms and groynes (leaving bends outside the present investigation). We obtain three schematic 1D tests, two schematic 2D tests and the actual river case study:

- Test 1: Uniform channel flow along a constant slope (1D)
- Test 2: Flow over a wavy bed without bottom friction (1D)
- Test 3: Flow over a sloped wavy bed with bottom friction (1D)
- Test 4: Flow over a sloped wavy bed with bottom friction and emerged groynes (2D)
- Test 5: Flow over a sloped wavy bed with bottom friction and submerged groynes (2D)
- Test 6: Case study: Elbe River from Lauenburg to Geesthacht (2D)

The topography and water levels for the five schematic tests are depicted in Fig. 2. For each test, the channel has a length  $L = 1000$  m and width  $W = 240$  m. At the upstream boundary a discharge,  $Q = 960 \text{ m}^3 \text{ s}^{-1}$ , is prescribed. At the downstream boundary the water level is fixed at  $\zeta = 8$  m, which is also the initial condition. The initial flow velocity is  $u = v = 0 \text{ m s}^{-1}$ . We define a reference bottom height  $h_{\text{ref}} = 4$  m on which all different geometry variations are superpositioned.

In all schematic tests, except for the uniform channel flow test, the channel bottom contains bed forms, which are described by a cosine function in the longitudinal  $x$ -direction. The bottom profile with the bed forms is described by the function:

$$h_b(x, y) = h_{\text{ref}} + A_b \cos(f_b x) \quad (38)$$

where  $h_b(x, y)$  is the bottom height (positive upwards) and  $A_b$  is the wave/bed form amplitude. The frequency  $f_b$  determines the length of the “bed forms” and is defined as  $f_b = 2\pi n_b / L$ , where  $n_b$  is the number of bed forms within the domain (see Table 1).

For the groyne tests (tests 4 and 5), seven cosine-shaped groynes – extending over half of the channel width – are superpositioned on top of the sloped wavy bottom, i.e. the main channel and groyne fields have the bottom geometry containing the bed forms from test 3. The length of the groyne fields  $L_{\text{gf}}$  was chosen to be 130 m (from groyne crest to groyne crest). At the position of the groynes, the topography is described by:

$$h_g(x, y) = h_{\text{ref}} + A_b \cos(f_b x) + A_g (1 + \cos(f_g (x - x_{\text{gs}}))) \quad (39)$$

where  $A_g$  is the groyne amplitude (half of the height) and  $x_{\text{gs}}$  is the  $x$ -coordinate where the cosine of each groyne starts. The frequency  $f_g$  follows from the chosen “width of the groyne”  $W_g$

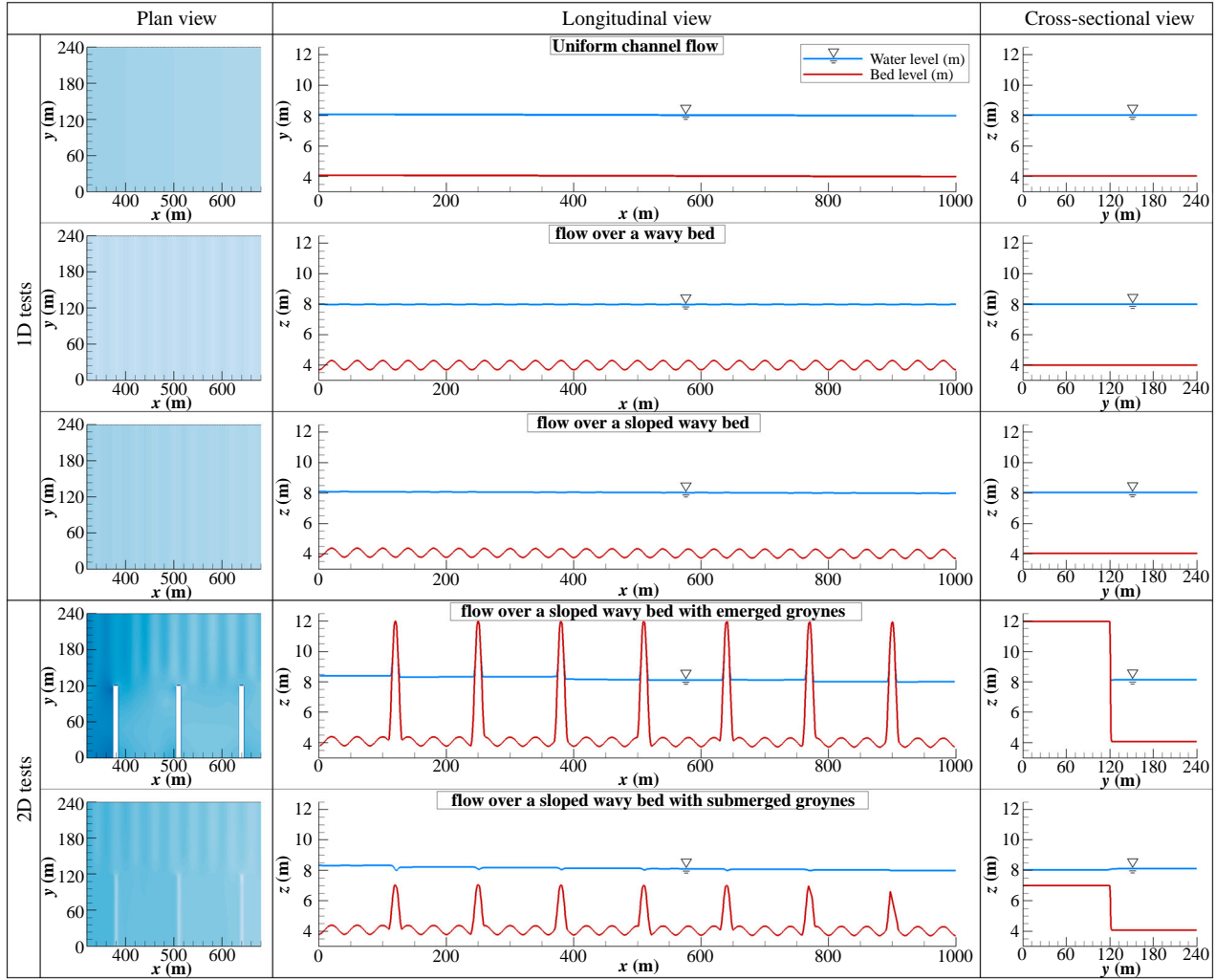


Figure 2 Plan view of water level (left), longitudinal view (middle) and cross-sectional view (right) of geometry and water level for tests 1–5. Longitudinal section taken at  $y = 60$  m. Lateral cross-section taken  $x = 510$  m

Table 1 Topography definitions for the five schematic tests

Test	Parameter												
	$L$ (m)	$W$ (m)	$h_{\text{ref}}$ (m)	$i_b$ (–)	$C_z$ ( $\text{m}^{1/2} \text{s}^{-1}$ )	$n_b$ (–)	$L_b$ (m)	$A_b$ (m)	$n_g$ (–)	$W_g$ (m)	$A_g$ (m)	$L_{gf}$ (m)	$F^{\text{max}}$ (–)
1	1000	240	4	$10^{-4}$	50	0	0	0	0	0	0	0	0.16
2	1000	240	4	0	$\infty$	25	40	0.3	0	0	0	0	0.17
3	1000	240	4	$10^{-4}$	50	25	40	0.3	0	0	0	0	0.17
4	1000	240	4	$10^{-4}$	50	25	40	0.3	7	20	4	130	0.36
5	1000	240	4	$10^{-4}$	50	25	40	0.3	7	20	1.5	130	0.7 <sup>a</sup>

<sup>a</sup> The maximum Froude number  $F^{\text{max}} \approx 1$  at the most upstream groyne for the submerged groyne case.

and is defined as  $f_g = 2\pi/W_g$ . The geometrical parameters of all the tests are presented in Table 1.

For all five schematic tests and all five advection schemes, we apply four recursively finer grids, to investigate the convergence properties and grid dependency of the schemes:

Resolution 1:  $\Delta x = 10$  m (4 cells per bed form)

Resolution 2:  $\Delta x = 5$  m (8 cells per bed form)

Resolution 3:  $\Delta x = 2.5$  m (16 cells per bed form)

Resolution 4:  $\Delta x = 1.25$  m (32 cells per bed form)

For the Elbe River test, four recursively finer resolutions ranging from  $\Delta x = 16$  m to  $\Delta x = 2$  m are applied.

For all tests, the time step is determined dynamically based on a prescribed Courant number  $C = |u^{\text{max}}| \Delta t / \Delta x$  and the maximum flow velocity  $u^{\text{max}}$ . For the first-order schemes, the



Courant number was fixed at  $C = 0.7$  and for the second-order schemes at  $C = 0.2$ , for maintaining stable solutions. The maximum Froude number  $F^{\max} = u/(gH)^{1/2}$  was also determined, yielding subcritical flow for all cases (Table 1). Only for the submerged groyne case, the flow locally becomes critical, with  $F^{\max} \approx 1$  at the first groyne; see Section 5.5.

#### 4.1 Uniform channel flow

For this test, the channel described above has a bottom slope  $i_b = 1 \times 10^{-4}$  (Table 1), sloping from  $z = 4.1$  m to  $z = 4$  m ( $h_{\text{ref}}$ ), giving the channel an equilibrium depth of  $H^{\text{eq}} = 4$  m. Combined with a Chézy bottom roughness  $C_z = 50 \text{ m}^{0.5} \text{ s}^{-1}$ , this results in a flow velocity  $u = C_z(Hi_b)^{1/2} = 1 \text{ m s}^{-1}$ , which matches the boundary condition described above. For this test, the advection term should be zero.

#### 4.2 Flow over a wavy bed

As described above, the channel bottom is described by a series of 25 cosines (wave length  $L_b = 40$  m) forming a wavy bed in the longitudinal  $x$ -direction (see Table 1). The amplitude of the bed forms is  $A_b = 0.3$  m, causing the total water depth to vary approximately from  $H = 3.7$  to  $4.3$  m. In the lateral  $y$ -direction, the bottom is constant. There is no general slope in the bed and the bottom friction is switched off:  $\gamma = 0$ . The bottom topography is shown in Fig. 2.

For the steady and inviscid flow over a smooth bottom at low Froude numbers the analytical solution can be computed based on the principles of mass and momentum conservation. For this simple flow situation, the momentum equation reduces to the Bernoulli equation upon integration (formally along a streamline):

$$u \frac{\partial u}{\partial x} + g \frac{\partial \zeta}{\partial x} = 0 \Rightarrow \quad (40)$$

$$\frac{1}{2}u^2 + g\zeta = E \quad (41)$$

where  $E$  is an integration constant, being the total (kinetic + potential) energy (divided by the density) in the system. It can be determined using the continuity equation and the boundary condition:  $E = g\zeta_{\text{BC}} - \frac{1}{2}(q/H_{\text{BC}})^2$ , where  $\zeta_{\text{BC}}$  is the water level prescribed e.g. at the downstream boundary and  $H_{\text{BC}}$  is its corresponding total water depth. This system of equations can be reduced to a single equation by substituting the steady 1D continuity equation  $u = Q/(WH) = q/H$  into the Bernoulli equation. After some algebra one ends up with the following cubic relation for the unknown total water depth  $H = H(x)$ , depending also on the bottom topography  $h = h(x)$  (e.g. Ricchiuto, 2015):

$$H^3 + \left(h - \frac{E}{2g}\right)H^2 + \frac{q^2}{2g} = 0 \quad (42)$$

This equation can be solved e.g. using Cardano's formula, or iteratively using Newton iterations. The solution for  $u$  is then obtained from  $u = q/H$ . The expressions for  $H$  and  $u$  are lengthy and therefore omitted, but as can be expected, they show an alternating wavy pattern. For this test, it is important that there should be no energy losses (zero bottom friction) and therefore no global backwater. The water level at the entrance of the channel should also be at  $\zeta = 8$  m. Any backwater in the experiment must come from numerical dissipation.

#### 4.3 Flow over a sloped wavy bed with bottom friction

In this test the uniform channel flow (with bottom friction) and the inviscid wavy bed test are combined. The bottom topography for the sloped wavy bed test is the same as for the wavy bed case, except for an additional downward slope of  $i_b = 1 \times 10^{-4}$ . Additionally, the bed friction is set to  $C_z = 50 \text{ m}^{1/2} \text{ s}^{-1}$ . The test settings are summarized in Table 1. The reference solution for this test was obtained by a step method integrating the momentum equation (now including bottom friction) from the downstream boundary upwards.

#### 4.4 Flow over a sloped wavy bed with emerged groynes

In this test, we add groynes to the sloped channel with wavy bed. Seven schematic groynes (described by cosine waves), with a groyne width in stream-wise direction  $W_g = 20$  m are added. The groynes extend over half of the channel width, i.e. the groynes are 120 m long and the groyne heads are cut vertically. The groyne fields between the groynes have a length  $L_{\text{gf}} = 130$  m (from groyne crest to groyne crest). In this first test, the groynes have a height of 8 m (twice the cosine amplitude of the groyne  $A_g = 4$  m) and are therefore emerged (Table 1 and Fig. 2).

#### 4.5 Flow over a sloped wavy bed with submerged groynes

For this test, only the cosine amplitude (half of the height) of the groynes is modified. The groynes are now 3 m high ( $A_g = 1.5$  m) and therefore approximately 1 m submerged. All other parameters for this test are identical to the emerged groynes test of the previous section (Table 1). The topography and water level is displayed in Fig. 2.

By comparing the results of the emerged and the submerged groynes case, one can investigate the effect of *lowering the groynes*, an important topic of discussion for river maintenance and flood protection issues (e.g. Busnelli, Schuurman, Sieben, van der Wal, & Hector, 2011).

#### 4.6 The Elbe River from Lauenburg to Geesthacht

The final test is the case study from which we derived the schematic tests. It concerns a reach of the Elbe River between the cities of Lauenburg and Geesthacht in Germany, which is

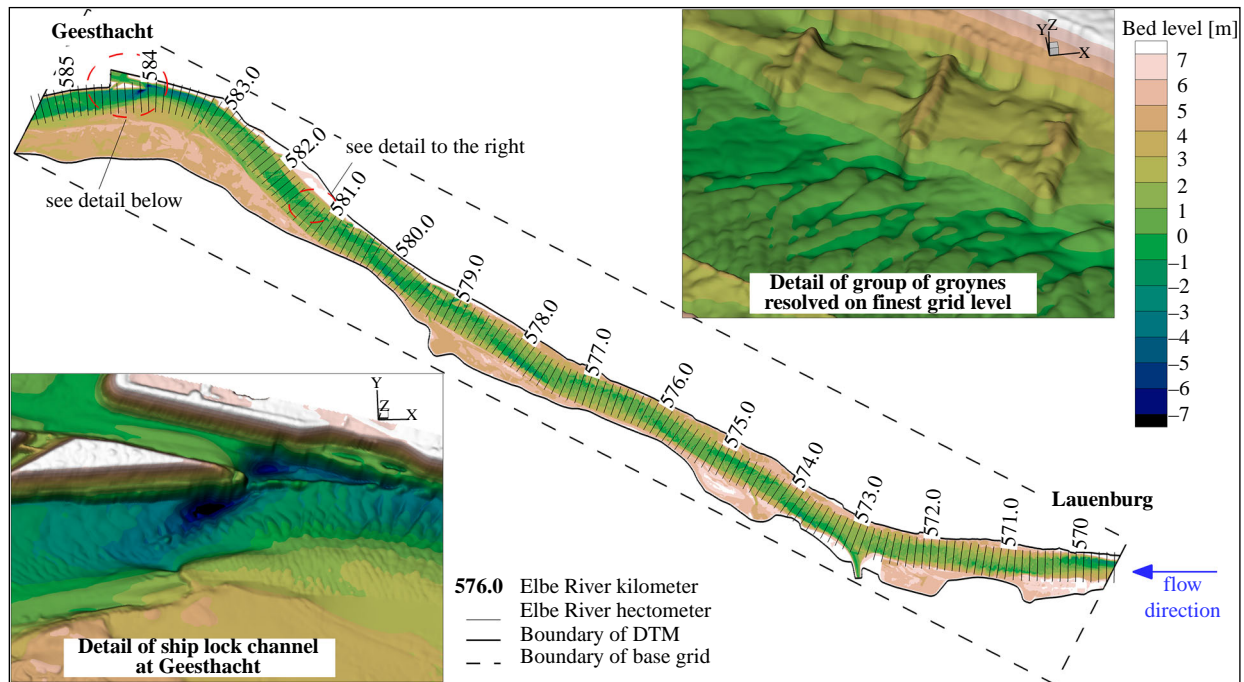


Figure 3 The Elbe River model: Digital Terrain Model (DTM) ( $2 \times 2$  m) for the Elbe River between the city of Lauenburg and the weir at Geesthacht. The 3D detail figures of the topography are 10 times vertically exaggerated, compared to the horizontal scale. Copyright © 2016 John Wiley & Sons, reprinted with permission from Platzek et al. (2016)

approximately 17 km long and – including the floodplains – 2.5 km wide (Fig. 3). The stretch contains natural bed forms with similar characteristics as the wavy bed cases and it contains groynes which are emerged near the bank and submerged near the groyne tip, for the chosen discharge. All parameters for this test were taken from Platzek et al. (2016).

## 5 Results

For each of the tests described in Section 4, for all five advection schemes and the four specified grid resolutions, we compute the contributions from bottom friction and the advection scheme to the total backwater, and the behaviour of these contributions with grid refinement. The different contributions to the backwater are computed numerically in the same way as for the analysis in Section 3, i.e. by integrating the corresponding terms (pressure, advection, bottom friction) over the length of the channel and scaling with  $g$ . For the 2D tests, an additional averaging over the width of the channel is performed. We express the backwater or head loss  $\Delta H$  at the inflow boundary in % of the backwater due to bottom friction over the same channel length. For test 2, with only bed forms and no bottom friction, the (analytical) backwater due to bottom friction from test 3 is used as a reference. For the two groyne tests and for the Elbe River case no analytic solution is available and the head loss from the runs with the smallest backwater is taken as the reference  $\Delta H^{\text{ref}}$ .

We have seen from the analysis in Section 3 that the artificial backwater contribution from the momentum advection discretization can be positive or negative. For this purpose, we

have chosen the backwater (or upstream water level difference) as the error norm and not a strictly-positive mathematical error norm (e.g.  $L_\infty$ ,  $L_1$  or  $L_2$ ), as it would not show the difference between a positive or negative backwater effect. To illustrate the order of convergence for tests 2 and 3 (where an analytical solution is available), we compute the  $L_\infty$  norm and the convergence rates  $p$  based on the  $L_1$  norm of the water level:

$$p^l = \frac{\log\left(\frac{L_1^{l-1}}{L_1^l}\right)}{\log(2)}, \quad \text{for } l = 2, 3, \dots, l^{\max} \quad (43)$$

with

$$L_1^l = \frac{1}{I^l} \sum_{i=1}^{I^l} |\zeta_i^l - \zeta_i^{\text{analytic}}| \quad (44)$$

where  $l$  is the grid level within the convergence study and  $I^l$  is the number of grid cells in  $x$ -direction on grid  $l$ . The convergence rate then gives the order of the scheme:  $O(\Delta x^p)$ .

### 5.1 Uniform channel flow

In this test, bottom friction causes the water level to be sloped downward along the channel from  $\zeta = 8.1$  m to  $\zeta = 8$  m, resulting in a constant total water depth  $H = 4$  m. Any deviation must come from errors made in the advection discretization or from the boundaries. The largest deviation of the water level at the upstream boundary, i.e. the numerical head loss or backwater, over all four resolutions, drops from  $-5 \times 10^{-4}$  m ( $\Delta x = 10$  m) to  $-5 \times 10^{-5}$  m. For the backwater  $\Delta H = 10$  cm over the

length of the channel, this is a spurious contribution of  $-0.5$  to  $-0.05\%$  due to discretization errors. No significant differences were found between the different advection schemes. For this test, it can therefore be concluded that – as expected – advection plays no significant role, and only bottom friction causes the backwater.

### 5.2 Flow over a wavy bed

For this test, the bottom friction is zero, but the bed level varies, causing gradual flow variation (due to the Bernoulli effect), which should occur without energy losses. As a reference for this test we take the backwater one would have over the same channel length, when bottom friction would be applied (see Section 5.3). Due to the additional resistance of the flow accelerations over the wavy bed, this backwater amounts to 10.22 cm (instead of the 10 cm for the uniform channel flow). Figure 4a shows the upstream head loss (or backwater) for the five advection schemes and the four grid resolutions. There is only a contribution from the advection term, as the bottom friction is zero.

It can be seen that, depending on the advection scheme, the numerical head loss can be as high as 36% of the backwater due to bottom friction, amounting to an artificial (additional) backwater of 3.6 cm. As was demonstrated using the analysis in Section 3, the FOU-EHC scheme shows (almost) no backwater. The very small backwater on the coarsest grid (0.1%) comes exclusively from the downstream boundary, due to a discrepancy in discretely representing the exact bed level at the boundary. Over the channel there is no additional build-up of the backwater. As expected, the second-order schemes perform somewhat better than their first-order counterparts. This can also be verified using the  $L_\infty$  norms and convergence rates given in Table 2.

### 5.3 Flow over a sloped wavy bed

Now we investigate to which extent the results from the previous test are also valid when combined with bottom friction (and a channel slope). For this test, the bed level variations interact with the quadratic bottom friction, resulting in a theoretical backwater and reference head loss of  $\Delta H^{\text{ref}} = 10.22$  cm (obtained using numerical integration of the equations on a  $\Delta x = 0.00125$  m grid). Figure 4b shows the total percentual upstream head loss  $100 \times (\zeta_{\text{upstream}} - \zeta_{\text{upstream}}^{\text{ref}}) / \Delta H^{\text{ref}}$  consisting of contributions both from the bed friction and from the advection term, for the different advection schemes and the four resolutions. The maximum head loss of 132% corresponds to 13.7 cm total head loss, instead of the 10.22 cm (100%) for the analytic solution. The results for the five schemes correspond to those of the previous test.

From these results one can conclude that the common consensus that numerical river models are dominated by a *global* balance between pressure gradient and bottom friction (in the

momentum equation) is not completely valid, due to the artificial backwater contribution from the advection approximation. For moderately coarse grids and for many advection schemes, the contribution of the advection term to the balance is of the same order as the backwater due to bottom friction. For the *local* balance in the momentum equation, the contribution from the advection term is even more dominant, as can be seen from Fig. 5, where we plotted the distribution along the channel centreline of the different acceleration terms in the momentum equation (summing up to zero), for the sloped wavy bed test, where we even reduced the bed form amplitude  $A_b$  to only 5 cm.

For completeness, the  $L_\infty$  norms and the convergence rates for this test have been included in Table 2. It can be seen that the inclusion of bottom friction has little effect on the convergence rates and that the targeted accuracy is attained by the second-order approximations.

### 5.4 Flow over a sloped wavy bed with emerged groynes

In this test, groynes are added to the test from Section 5.3. The groynes have a height of 6 m above the bed and are therefore emerged. We now inspect the effect of such groynes on the backwater and, more specifically, the dependency on the advection scheme. The total head loss again has two contributions: bottom friction and advection. Figure 4c shows the percentual head loss for the five schemes. As no analytical solution is available for this test, we have taken the advection scheme with the least total head loss at the upstream boundary as the reference:  $\Delta H^{\text{ref}} = 35$  cm, as computed by the FOU-EHC scheme on the  $\Delta x = 1.25$  m grid (corresponding to a percentual head loss  $\Delta H = 100\%$ ). A 20% head loss in the figure thus corresponds to 7 cm of additional head loss on top of the 35 cm.

From the figure three things can be noted. First, one can see that with an increased head loss due to advection, the head loss due to bottom friction decreases. Second, the convergence behaviour of the schemes is different. In particular the FOU-EHC scheme shows very little variation over the grids. Finally, it appears that the different schemes converge to different solutions. In particular the fine-grid results of the FOU and SOU scheme differ from the results of the other three schemes.

The switch from a first- to a second-order advection scheme shows moderate influence on the backwater. The effect on the flow velocity and on the emergence of turbulent eddies is much greater. In Fig. 6, the  $z$ -component of the vorticity  $\omega = \nabla \times \mathbf{u}$  is displayed as projected on the free surface, for the FOU-MC-E and SOU-MC-E schemes for the three finest grids. It can be seen that with the first-order scheme, vortex shedding is much less pronounced than with the second-order scheme, in particular on the coarser grids.

### 5.5 Flow over a sloped wavy bed with submerged groynes

In this test, the groynes from the previous test are lowered such that they become submerged. The maximum Froude number

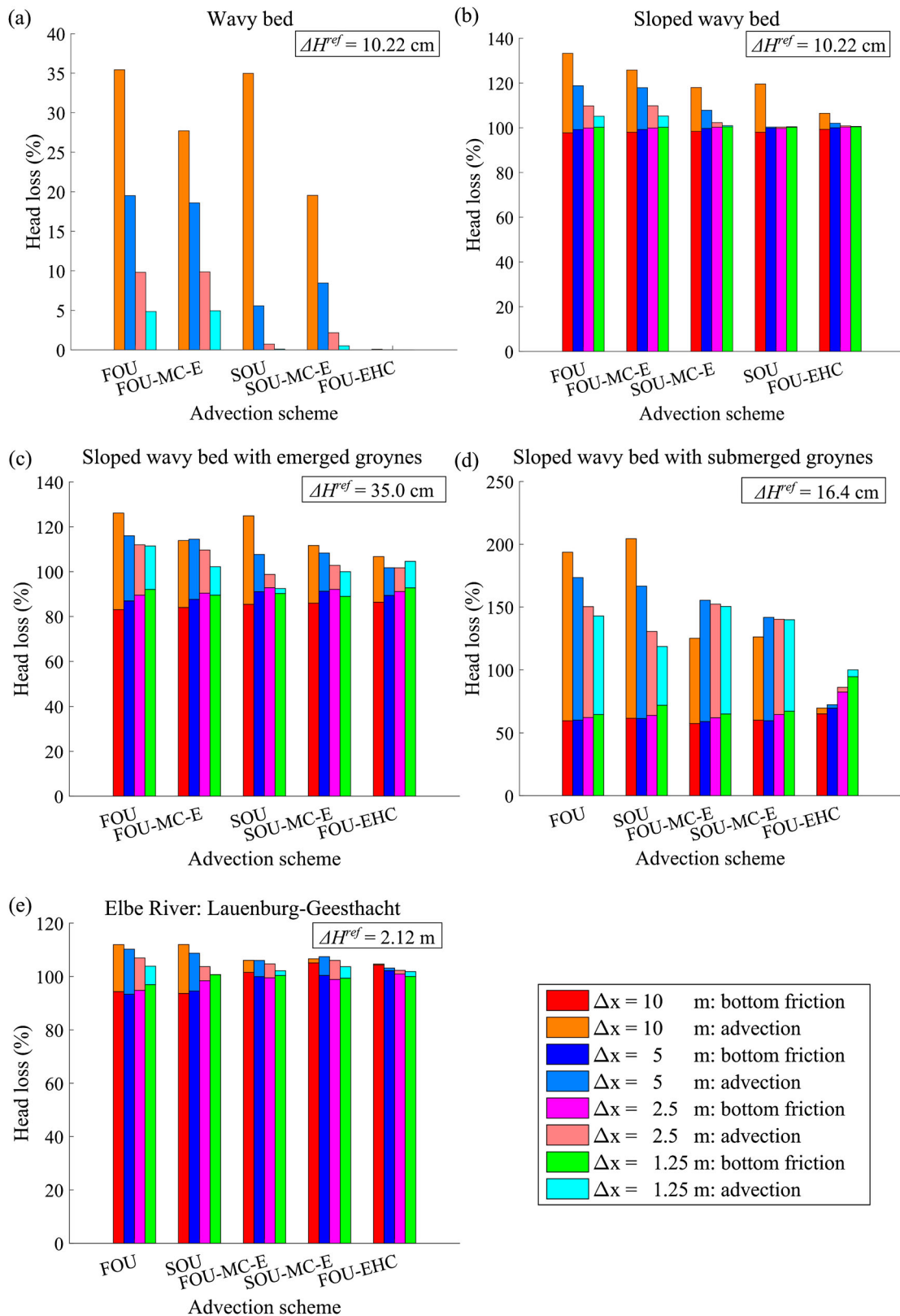
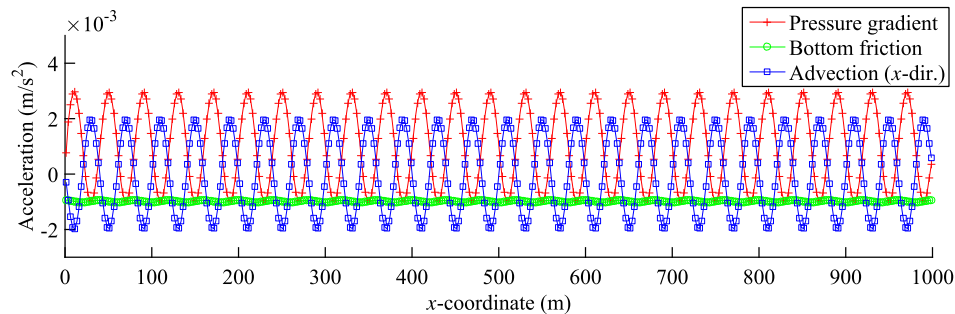


Figure 4 Percentual head loss for test cases 2–6, for all five advection schemes and all four grid resolutions. Displayed is the total head loss as a sum of the head loss due to bottom friction and the head loss due to advection for: (a) flow over a wavy bed; (b) flow over a sloped wavy bed; (c) flow over a sloped wavy bed with emerged groynes; (d) flow over a sloped wavy bed with submerged groynes; (e) the Elbe River from Lauenburg to Geesthacht. The reference head losses  $\Delta H^{ref}$  are also included



Table 2  $L_\infty$  norms and convergence rates  $p$  for the different advection schemes, for tests 2 and 3 (flow over a wavy bed and over a sloped wavy bed)

Advection scheme	Grid resolution $\Delta x$ (m)	Test 2: wavy bed		Test 3: sloped wavy bed	
		$L_\infty$ norm (m)	Convergence rate $p$	$L_\infty$ norm (m)	Convergence rate $p$
FOU	10	$4.2 \times 10^{-2}$	—	$4.0 \times 10^{-2}$	—
	5	$2.3 \times 10^{-2}$	0.98	$2.2 \times 10^{-2}$	0.97
	2.5	$1.2 \times 10^{-2}$	1.06	$1.1 \times 10^{-2}$	1.05
	1.25	$5.7 \times 10^{-3}$	1.05	$5.6 \times 10^{-3}$	1.04
FOU-MC-E	10	$3.4 \times 10^{-2}$	—	$3.3 \times 10^{-2}$	—
	5	$2.2 \times 10^{-2}$	0.75	$2.1 \times 10^{-2}$	0.75
	2.5	$1.1 \times 10^{-2}$	0.99	$1.1 \times 10^{-2}$	0.98
	1.25	$5.8 \times 10^{-3}$	1.03	$5.7 \times 10^{-3}$	1.02
FOU-EHC	10	$6.1 \times 10^{-3}$	—	$6.4 \times 10^{-3}$	—
	5	$3.1 \times 10^{-3}$	0.93	$3.3 \times 10^{-3}$	0.93
	2.5	$1.6 \times 10^{-3}$	0.98	$1.6 \times 10^{-3}$	0.98
	1.25	$7.9 \times 10^{-4}$	0.99	$8.4 \times 10^{-4}$	0.99
SOU	10	$3.7 \times 10^{-2}$	—	$3.6 \times 10^{-2}$	—
	5	$6.1 \times 10^{-3}$	2.92	$6.1 \times 10^{-3}$	2.87
	2.5	$8.9 \times 10^{-4}$	2.79	$9.5 \times 10^{-4}$	2.72
	1.25	$2.3 \times 10^{-4}$	2.12	$1.9 \times 10^{-4}$	2.17
SOU-MC-E	10	$2.6 \times 10^{-2}$	—	$2.5 \times 10^{-2}$	—
	5	$1.0 \times 10^{-2}$	1.45	$1.0 \times 10^{-2}$	1.43
	2.5	$2.6 \times 10^{-3}$	2.02	$2.6 \times 10^{-3}$	1.96
	1.25	$6.3 \times 10^{-4}$	2.10	$6.6 \times 10^{-4}$	1.95

Figure 5 Different acceleration terms in the momentum equation along the channel centreline for the sloped wavy bed test with a reduced bed form amplitude  $A_b = 0.05$  m

for this case occurs at the groyne crest near the groyne head. Depending on the chosen advection scheme (and the resulting backwater) we obtain  $F^{\max} \approx 0.7$ . Only at the first groyne, the flow becomes critical with  $F^{\max} \approx 1$ , see also Table 1. This is due to the fact that a uniform discharge is specified over the whole width of the upstream boundary, resulting in a higher specific discharge over the first groyne.

Figure 4d shows the percentual head loss for the different advection schemes and grid resolutions. The reference solution for this test was taken to be the solution obtained with the FOU-EHC scheme on the finest grid resolution with  $\Delta x = 1.25$  m, with a total head loss of 16.4 cm, corresponding to a 100% head loss in the figure. This means that the 277% head loss in the figure – as obtained using the FOU scheme on the coarsest grid – gives a total head loss of 45.4 cm, i.e. an additional backwater of 29 cm over 1000 m of channel length, due to the advection discretization.

Again, we can deduce several things from the figure. First, the head losses for this test are much larger than for the previous tests. Second, it can be seen that on the finer grids the FOU, FOU-MC-E and SOU-MC-E schemes provide similar head losses  $\Delta H \approx 140$ –150%. We know that, in reality, vertical recirculation zones emerge behind the groynes, dissipating energy. This mechanism is, of course, not incorporated in our 2D, depth-averaged model. In civil engineering methods, these losses are commonly parameterized using Carnot losses for sudden expansions (see e.g. Chanson, 2004). From the analysis in Section 3, we know that the FOU scheme gives exactly the Carnot loss for any (discrete) velocity variation. It appears that both momentum conservative schemes also tend towards this result. Additionally, it can be noted that these two schemes also show relatively little dependence on the grid resolution.

Finally, it can be seen that the FOU-EHC scheme provides a reduction in the backwater for the coarser grids. From the



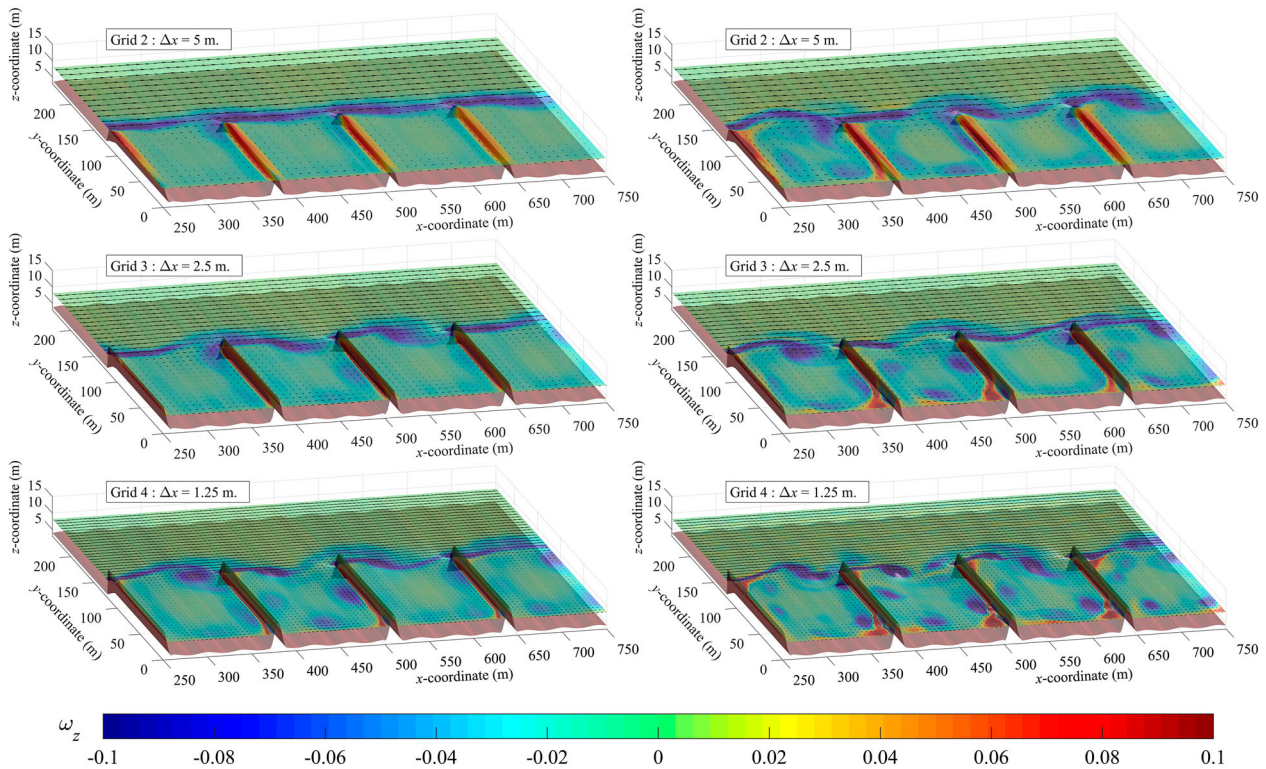


Figure 6 Flow around emerged groynes:  $z$ -component of the vorticity  $\omega$  (unit  $\text{s}^{-1}$ ) around groynes 5, 6 and 7, superimposed on the free surface level, for the FOU-MC-E (left) and SOU-MC-E (right) advection scheme, for the three finest grids

analysis, we know that the scheme does not give any head losses related to the velocity gradients. Therefore, the backwater is much less than for the other schemes. The increase in head losses with increased grid resolution, most likely comes from the better representation of the local accelerations over the groynes and therefore the increased bottom friction contribution. The advection contribution only varies between 4 and 8% over the grids. The FOU-MC-E scheme gives a significantly larger backwater than the FOU-EHC scheme and depending on the resolution a larger or smaller backwater than the FOU scheme (confirming the results from Section 3). It can also be seen that it shows relatively little variation over the range of grid resolutions.

By comparing the results with the test with emerged groynes, one can investigate the effect of lowering the groynes in a river section (see e.g. Busnelli et al., 2011). Computing the difference in water levels for the two flow situations, for the different advection schemes and grid resolutions, the effect of lowering the groynes can be found to be in the range of 9–23 cm. Considering the fact that often river engineering projects involve man-induced modifications which result in water level changes of several centimetres to decimetres and that the river engineers commonly need to provide water level predictions with an accuracy below 5 cm, this result can be considered worrying.

### 5.6 Case study: Elbe River from Lauenburg to Geesthacht

Finally, we consider the actual case study from which we deduced the schematic tests and their topographical

characteristics. Again, we apply all five advection schemes on the four grid resolutions, and inspect the differences in the total backwater at the upstream boundary. From Fig. 4e one can see that the variation in total head loss over the schemes is less than for the schematic cases: the contribution from the bottom friction is more dominant for this case.

Nonetheless, the maximum difference of 10.4% (of a total backwater of 2.12 m over 17 km) corresponds to a water level difference of 22 cm, from which one can again conclude that the uncertainty due to the advection scheme is quite significant. This needs to be counteracted by a reduced bottom friction, which may modify the flow patterns, specifically in shallow areas, reducing the reliability and applicability of the model, in particular for possible morphodynamic computations, relying on accurate bottom shear stress predictions.

However, the variation over the grids for the two momentum-conservative schemes and for the FOU-EHC scheme is relatively small, rendering them more reliable than the FOU and SOU schemes. It can thus be concluded that the order of the scheme is not the essential property for an advection scheme to be accurate and reliable in river applications for backwater assessment.

## 6 Discussion

It was shown that, for quasi-steady river flow over variable topography, the *local balance* in the momentum equation is dominated by the pressure gradient and advection term and not

by the pressure gradient and bottom friction. Due to the errors in the advection scheme, even the contribution to the *global balance* may be substantial, depending on the chosen advection scheme and grid resolution. Therefore, the common consensus that numerical river models are dominated by a balance between pressure (or free-surface) gradient and bottom friction is often invalid. Already for relatively small bottom variations, the global contribution to the backwater due to inaccuracies of the advection scheme may be of the same order of magnitude as that from bottom friction.

The effect of numerical errors on the energy head and backwater was investigated from an integral viewpoint. A more local approach (per cell/edge) is applied in research on energy-balanced schemes over (discontinuous) topography; see e.g. Tadmor and Zhong (2008), Fjordholm, Mishra, and Tadmor (2011), Murillo and García-Navarro (2013) and Bruwier, Archambeau, Erpicum, Pirotton, and Dewals (2016). A comparison of both approaches may yield interesting similarities and offer new insights in the effectivity of the different discretizations near bottom discontinuities.

We applied a range of practically-feasible grid resolutions, capturing the geometrical variation with a very limited number of cells, as the computational resources are often limited for large-scale river applications. In comparison with classical test cases such as the “*subcritical flow over a bottom bump*”, we considered a series of such bumps (and groynes), to allow for an accumulation of the possible numerical/artificial backwater that is introduced by the errors in the advection discretization.

The backwater effect for the flow over bed forms and influenced by groynes was studied. However, as any variation of the bathymetry may lead to artificial advection effects, it is very likely that this is also the case for the flow through bends, where similar investigations could be realized (e.g. Blanckaert, 2010; Blanckaert & Graf, 2004; Stelling, 2012; van Balen, Uijttewaalt, & Blanckaert, 2010). Also, in this study we restrict ourselves to quasi-steady flow with stationary boundary conditions. As can be seen from the presented results, the findings from this work also apply for mildly instationary flow situations.

In the present work a number of basic advection schemes were tested. It may be of interest to also apply other advection approximations to the presented set of test cases, inspired by a real-world river application, with the focus on the head loss and backwater. Additionally, the investigations from this work can be realized on unstructured (triangular) or locally-refined grids, where the discretization errors from the advection scheme will interact with errors from the grid structure.

## 7 Conclusions

We provided a new interpretation of discretization errors in numerical river models, introducing the concept of artificial backwater. The artificial/numerical backwater effect due to the momentum advection approximation was quantified for three

first-order advection schemes using a 1D analysis and verified using a sequence of 2D numerical experiments for the same schemes and for two second-order accurate extensions.

We demonstrated that a scheme designed for maintaining constant energy head can indeed compute the flow over variable topography with minimal energy losses. It was also shown that, in agreement with the conclusions from Kramer and Stelling (2008); Stelling and Duinmeijer (2003), the artificial backwater for the momentum-conservative scheme cannot be controlled. The scheme gives an energy loss (positive backwater contribution) at expansions and an energy gain (negative backwater contribution) for contractions. However, the momentum-conservative scheme yields a smaller artificial backwater than the non-conservative (standard) first-order upwind (FOU) scheme.

These findings are confirmed by the numerical experiments, where the contributions to the global backwater from bottom friction and from the advection scheme have been computed. The scheme with energy-head constancy indeed shows very little to no backwater, but unfortunately shows this property also for flows where losses might be expected, such as for the flow over groynes. The non-conservative first-order upwind scheme was found to cause an artificial backwater effect that could be as high as 35% of the backwater due to bottom friction. In agreement with the 1D analysis, the momentum-conservative scheme shows less backwater than the FOU scheme.

Tests with the second-order extensions of the schemes show that the non-conservative second-order scheme does converge faster than the FOU scheme, but on coarser grids, the backwater is equal to or even larger than with the FOU scheme. First-order advection schemes that adhere to physical principles, such as momentum conservation or energy-head constancy along streamlines, give less artificial backwater than a higher-order scheme that does not adhere to such principles.

For the flow over and around groynes, the total head loss for the different advection schemes and resolutions varies with as much as a factor of two, corresponding to several decimetres of water level difference. The lowering of the groynes resulted in a decrease in water levels in the range of 9–23 cm, depending on the advection scheme and the grid resolution, rendering these choices very relevant in engineering projects.

At present, most river computations employ relatively coarse grids, where the topography is resolved with limited resolution and the size of the artificial backwater considerably depends on the chosen advection scheme. From the semi-implicit, staggered grid, finite difference/finite volume schemes investigated in the present work – for such low-resolution computations – the authors recommend the use of a momentum-conservative first-order scheme or a scheme with energy-head constancy, for their efficiency and insensitivity to the grid resolution. Only for higher resolutions – where accurate flow patterns need to be resolved (e.g. including vortex shedding) – a second-order momentum-conservative scheme is recommended.

## Acknowledgments

The authors express their gratitude to the two anonymous reviewers for their suggestions, greatly improving the quality of the manuscript.

## Notation

$A$	= amplitude (m)
$c$	= wave celerity ( $\text{m s}^{-1}$ )
$C$	= Courant number (–)
$C_z$	= Chézy bottom friction coefficient ( $\text{m}^{1/2} \text{s}^{-1}$ )
$E$	= total energy (normalized with density $\rho$ ) ( $\text{m}^2 \text{s}^{-2}$ )
$f$	= frequency ( $\text{s}^{-1}$ )
$F$	= Froude number (–)
$F_u$	= explicit contribution of $u$ -momentum ( $\text{m s}^{-1}$ )
$F_v$	= explicit contribution of $v$ -momentum ( $\text{m s}^{-1}$ )
$g$	= gravity acceleration ( $\text{m s}^{-2}$ )
$h$	= bed level (m)
$H$	= total water depth (m)
$i$	= cell index in $x$ -direction (–)
$i_b$	= bed slope (–)
$I$	= number of cells in $x$ -direction (–)
$j$	= cell index in $y$ -direction (–)
$l$	= grid refinement level (–)
$L$	= length (m)
$M$	= normalized momentum integral (m)
$n$	= time step number (–)
$n_b$	= number of bed forms (–)
$n_g$	= number of groynes (–)
$p$	= convergence rate (–)
$q$	= specific discharge ( $\text{m}^2 \text{s}^{-1}$ )
$Q$	= total discharge ( $\text{m}^3 \text{s}^{-1}$ )
$r$	= slope ratio in limiter (–)
$u$	= flow velocity in $x$ -direction ( $\text{m s}^{-1}$ )
$v$	= flow velocity in $y$ -direction ( $\text{m s}^{-1}$ )
$W$	= width (m)
$x$	= primary horizontal coordinate (m)
$y$	= secondary horizontal coordinate (m)
$z$	= vertical coordinate (m)
$\alpha$	= advection coefficient (–)
$\gamma$	= bottom friction coefficient (–)
$\Gamma$	= grid edge indicator (–)
$\Delta H$	= head loss/backwater (m)
$\Delta t$	= time step size (s)
$\Delta x$	= grid size in $x$ -direction (m)
$\Delta y$	= grid size in $y$ -direction (m)
$\zeta$	= water level (m)
$\lambda$	= backwater ratio (–)
$\psi$	= limiter function (–)
$\omega$	= vorticity ( $\text{s}^{-1}$ )
$\Omega$	= grid cell indicator (–)

## References

- Blancaert, K. (2010). Topographic steering, flow recirculation, velocity redistribution, and bed topography in sharp meander bends. *Water Resources Research*, 46(9), 1–23.
- Blancaert, K., & Graf, W. H. (2004). Momentum transport in sharp open-channel bends. *Journal of Hydraulic Engineering*, 130(3), 186–198.
- Blumberg, A. F., & Mellor, G. L. (1987). A description of a three-dimensional coastal ocean circulation model. In N. Heaps (Eds.), *Three-dimensional coastal ocean models* (pp. 1–16). Washington, DC: American Geophysical Union.
- Brunner, G. W. (2016). *HEC-RAS river analysis system, hydraulic reference manual 5.0* (538 pp). Davis, CA: US Army Corps of Engineers.
- Bruwier, M., Archambeau, P., Erpicum, S., Piroton, M., & Dewals, B. (2016). Discretization of the divergence formulation of the bed slope term in the shallow-water equations and consequences in terms of energy balance. *Applied Mathematical Modelling*, 40, 7532–7544.
- Busnelli, M., Schuurman, F., Sieben, A., van der Wal, M., & Hector, H. (2011). Morphodynamic responds of groyne fields to the lowering of crest level of the groynes in the Waal River, The Netherlands. In *River, coastal and estuarine morphodynamics: RCEM2011* (pp. 1450–1463). Beijing: Tsinghua University Press.
- Caleffi, V., & Valiani, A. (2009). Well-balanced bottom discontinuities treatment for high-order shallow water equations WENO scheme. *Journal of Engineering Mechanics*, 135(7), 684–696.
- Caleffi, V., Valiani, A., & Li, G. (2016). A comparison between bottom-discontinuity numerical treatments in the DG framework. *Applied Mathematical Modelling*, 40, 7516–7531.
- Canestrelli, A., & Toro, E. F. (2012). Restoration of the contact surface in FORCE-type centred schemes II: Non-conservative one- and two-layer two-dimensional shallow water equations. *Advances in Water Resources*, 47, 76–87.
- Casulli, V. (1990). Semi-implicit finite difference methods for the two-dimensional shallow water equations. *Journal of Computational Physics*, 86(1), 56–74.
- Casulli, V., & Cattani, E. (1994). Stability, accuracy and efficiency of a semi-implicit method for three-dimensional shallow water flow. *Computers & Mathematics with Applications*, 27(4), 99–112.
- Casulli, V., & Walters, R. (2000). An unstructured grid, three-dimensional model based on the shallow water equations. *International Journal for Numerical Methods in Fluids*, 32(3), 331–348.
- Chanson, H. (2004). *The hydraulics of open channel flow: an introduction* (Second ed.). Oxford: Butterworth-Heinemann.
- Chanson, H. (2009). Development of the Bélanger equation and backwater equation by Jean-Baptiste Bélanger (1828). *Journal of Hydraulic Engineering*, 135(3), 159–163.



- Deltares. (2011). *Delft3D-FLOW: Simulation of multi-dimensional hydrodynamic flows and transport phenomena, including sediments. User Manual* (672 pp). Delft.
- DHI. (2011). *MIKE 21 C curvilinear model, scientific documentation. Mike by DHI* (112 pp). Hørsholm.
- Fjordholm, U. S., Mishra, S., & Tadmor, E. (2011). Well-balanced and energy stable schemes for the shallow water equations with discontinuous topography. *Journal of Computational Physics*, 230(14), 5587–5609.
- Fringer, O. B., Gerritsen, M., & Street, R. L. (2006). An unstructured-grid, finite-volume, nonhydrostatic, parallel coastal ocean simulator. *Ocean Modelling*, 14, 139–173.
- Kernkamp, H. W. J., van Dam, A., Stelling, G. S., & de Goede, E. D. (2011). Efficient scheme for the shallow water equations on unstructured grids with application to the continental shelf. *Ocean Dynamics*, 61(8), 1175–1188.
- Kleptsova, O., Pietrzak, J., & Stelling, G. (2012). On a momentum conservative z-layer unstructured C-grid ocean model with flooding. *Ocean Dynamics*, 54–55, 18–36.
- Kramer, S. C., & Stelling, G. S. (2008). A conservative unstructured scheme for rapidly varied flows. *International Journal for Numerical Methods in Fluids*, 58(2), 183–212.
- Murillo, J., & García-Navarro, P. (2013). Energy balance numerical schemes for shallow water equations with discontinuous topography. *Journal of Computational Physics*, 236, 119–142.
- Noelle, S., Xing, Y., & Shu, C. W. (2007). High-order well-balanced finite volume WENO schemes for shallow water equation with moving water. *Journal of Computational Physics*, 226(1), 29–58.
- Perot, B. (2000). Conservation properties of unstructured staggered mesh schemes. *Journal of Computational Physics*, 159, 58–89.
- Platzeek, F. W., Stelling, G. S., Jankowski, J. A., Patzwahl, R., & Pietrzak, J. D. (2016). An efficient semi-implicit subgrid method for free-surface flow on hierarchical grids. *International Journal for Numerical Methods in Fluids*, 80(12), 715–741.
- Ricchiuto, M. (2015). An explicit residual based approach for shallow water flows. *Journal of Computational Physics*, 280, 306–344.
- Stelling, G. S. (2012). Quadtree flood simulations with sub-grid digital elevation models. *Proceedings of the ICE - Water Management*, 165(WM10), 567–580.
- Stelling, G. S., & Duinmeijer, S. P. A. (2003). A staggered conservative scheme for every Froude number in rapidly varied shallow water flows. *International Journal for Numerical Methods in Fluids*, 43, 1329–1354.
- Tadmor, E., & Zhong, W. (2008). Energy-preserving and stable approximations for the two-dimensional shallow water equations. In H. Munthe-Kaas & B. Owren (Eds.), *Mathematics and computation, a contemporary view. Proceedings of the 2006 Abel symposium held in Alesund*, 67–94. Springer.
- Toro, E. F., & García-Navarro, P. (2007). Godunov-type methods for free-surface shallow flows: A review. *Journal of Hydraulic Research*, 45(6), 736–751.
- van Balen, W., Uijttewaalt, W. S. J., & Blanckaert, K. (2010). Large-eddy simulation of a curved open-channel flow over topography. *Physics of Fluids*, 22, 18 pp.
- Volp, N. D., van Prooijen, B. C., & Stelling, G. S. (2013). A finite volume approach for shallow water flow accounting for high-resolution bathymetry and roughness data. *Water Resources Research*, 49(7), 4126–4135.
- Zhang, D., Jiang, C., Liang, D., & Cheng, L. (2015). A review on TVD schemes and a refined flux-limiter for steady-state calculations. *Journal of Computational Physics*, 302, 114–154.